ORIGINAL PAPER

Sulfur oxidation state and solubility in silicate melts

Julien Boulliung[1] · Bernard J. Wood[1]

Abstract

We have determined the solubility of sulfur (S) as sulfide (S^{2-}) for 13 different natural melt compositions at temperatures of 1473–1773 K under controlled conditions of oxygen and sulfur fugacities (fO_2 and fS_2, respectively). The S and major element contents of the quenched glasses were determined by electron microprobe. The sulfide capacity parameter (C_{S2-}) was used to express S^{2-} solubility as a function of the oxygen and sulfur fugacities according to the equation: $\log C_{S2-} = \log S_{melt}(wt\%) + 0.5 \log \left(\frac{fO_2}{fS_2} \right)$. Sulfide capacities of silicate melts were found to increase with temperature and the FeO content of the melt. We combined our sulfide data at 1473–1773 K with (O'Neill and Mavrogenes, J Petrol 43:1049–1087, 2002) results at 1673 K, and obtained by stepwise linear regression the following equation for sulfide capacity $\log C_{S2-} = 0.225 + \left(25237X_{FeO} + 5214X_{CaO} + 12705X_{MnO} + 19829X_{K_2O} - 1109X_{Si_{0.5}O} - 8879 \right)/T$. X_{MO} is the mole fraction of the oxide of M on a single-oxygen basis, and T is in Kelvin. The sulfide capacity equation was combined with sulfate capacity (C_{S6+}) data for similar compositions and at the same temperatures (Boulliung and Wood, Geochim Cosmochim Acta 336:150–164, 2022), to estimate the S redox state (S^{6+}/S^{2-} ratio) as a function of melt composition, temperature and oxygen fugacity. Results obtained are in good agreement with earlier measurements of S^{6+}/S^{2-} for basaltic and andesitic compositions. We observe a significant increase, however, relative to FMQ of the oxygen fugacity of the S^{2-} to S^{6+} transition as temperature is lowered from 1773 to 1473 K. We used our results to simulate sulfur-degassing paths for basaltic compositions under various redox conditions (FMQ −2 log fO_2 units to FMQ + 2). The calculations indicate that, given an initial concentration of 0.12 wt% S in an ascending melt at 250 MPa, most of the S (> 80%) will be degassed before the magma reaches 100 MPa pressure.

Keywords Sulfur oxidation state in melts · Sulfur solubility in melts · Sulfur degassing · Sulfide in melts · Sulfate in melts

Introduction

Sulfur (S) is the 11th most abundant element in the Silicate Earth and is one of the major volatiles in magmas being degassed principally from volcanic systems as SO_2 and H_2S. Such volcanism is the principal means by which sulfur is transferred from the solid Earth to the crust, oceans and atmosphere where it is an essential nutrient in sulfate metabolism on the seafloor and, as SO_2, may have

medium-term cooling effects on global climate. Sulfur is also a major component of magmatic ore deposits providing sulfide hosts for economically important elements such as Ni, Cu, Pt, and Au. The behavior of sulfur in the environment depends greatly on its oxidation state, which varies from S^{2-} (basaltic melts) to S^0 (native sulfur) to S^{4+} (SO_2 gas) and S^{6+} (seawater sulfate and oxidized melts). Because of its abundance and variable oxidation state, redox processes involving sulfur frequently involve and require interaction with iron (e.g., Nash et al. 2019) during, for example, iron sulfide precipitation and SO_2 degassing. Given, therefore, its environmental and economic importance, the behavior of sulfur in volcanic systems, through which it is transferred from mantle to crust and the external environment, is an issue of major importance. For this reason, a large number of experimental and theoretical studies have addressed sulfur oxidation state and solubility in natural and synthetic silicate melts. In this paper, we

✉ Bernard J. Wood
  bernie.wood@earth.ox.ac.uk

  Julien Boulliung
 julien.boulliung@earth.ox.ac.uk

1 Department of Earth Sciences, University of Oxford, South Parks Road, Oxford OX1 3AN, UK

present new experimental data on sulfide (S^{2-}) solubility in a wide range of melts and combine the results with earlier experimental studies to present a comprehensive model for sulfur behavior at low-to-moderate (crustal) pressures and high temperatures (1323–1773 K).

Experiments performed to date indicate that sulfur occurs almost exclusively in 2 oxidation states S^{2-} and S^{6+} in natural silicate melts (e.g., Fincham and Richardson 1954; Jugo et al. 2010; Nash et al. 2019). There is some evidence of the existence of S^0 (Matjuschkin et al. 2016) and S^{4+} (Metrich et al. 2009) at high pressures (0.4–1.6 GPa), but these oxidation states may probably be neglected at the lower pressures relevant to volcanism and ore deposition. In nature, under the reducing conditions ($fO_2 <$ fayalite-magnetite-quartz buffer, FMQ) relevant to much basaltic volcanism, S is dissolved in the melts mainly as sulfide S^{2-} (Carroll and Webster 1994; O'Neill and Mavrogenes 2002; Scaillet et al. 2003; Moretti and Ottonello 2005; Nash et al. 2019). Under more oxidizing conditions, at $fO_2 > \sim$ FMQ + 1 log fO_2 unit, S is mainly dissolved as sulfate (SO_4^{2-}) (e.g., Fincham and Richardson 1954; Carroll and Webster 1994; Jugo et al. 2005, 2010; Behrens and Gaillard 2006; Nash et al. 2019). Under intermediate redox conditions at about and just above FMQ, both sulfide and sulfate species are present (Wallace and Carmichael 1994; Wilke et al. 2008; Jugo et al. 2010; Nash et al. 2019).

## Sulfur dissolution in silicate melts at 1 atm pressure

In their classic paper, Fincham and Richardson (1954) showed that the dissolution of sulfur in silicate melts at 1-atmosphere pressure follows two end-member reactions, which depend on oxygen and sulfur fugacities. At oxygen fugacities below approximately, depending on composition, FMQ, sulfur dissolves as S^{2-} replacing O^{2-} in the melt:

$$\frac{1}{2}S_{2(gas)} + O^{2-}_{melt} = \frac{1}{2}O_{2(gas)} + S^{2-}_{melt} \tag{1}$$
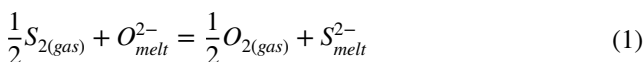
With a small amount of algebra, we can show from the equilibrium constant for (1) that the S^{2-} content of the melt $[S^{2-}]$ depends on the ratio of oxygen to sulfur fugacities and a combined compositional and temperature term denoted the sulfide "capacity" C_{S2-} (2):

$$\log\left[S^{2-}\right] = \log C_{S2-} + \log\left(\frac{fS_2}{fO_2}\right)^{1/2} \tag{2}$$

At high oxygen fugacities, at least 1–2 log fO_2 units above FMQ, sulfur dissolves predominantly as SO_4^{2-} according to the reaction (3):

$$\frac{1}{2}S_{2(gas)} + \frac{3}{2}O_{2(gas)} + O^{2-}_{melt} = SO^{2-}_{4(melt)} \tag{3}$$
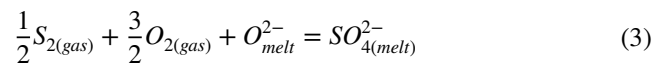
In this case, rearranging the equilibrium constant and introducing the composition-temperature term known as the sulfate capacity (C_{S6+}) leads to Eq. (4):

$$\log\left[SO_4^{2-}\right] = \log C_{S^{6+}} + \frac{1}{2}\log fS_2 + \frac{3}{2}\log fO_2 \tag{4}$$

Sulfide capacities have been determined for a range of compositions and temperatures at 1 atm pressure (Buchanan and Nolan 1979; Fincham and Richardson 1954; O'Neill and Mavrogenes 2002). Information on sulfate capacities was, however, much more sparse until the recent papers by O'Neill and Mavrogenes (2022) and Boulliung and Wood (2022) which have provided a strong basis on which to develop realistic models of S behavior in natural melts at low pressures. We should also mention the pioneering attempts to produce models of S speciation and solubility (e.g., Moretti and Ottonello 2005) which may now be improved with the recent proliferation of experimental constraints.

Given that we now have enough data to formulate an equation for sulfate capacity at low pressure that covers the compositional range from basanite, through iron and titanium-rich lunar basalt to andesite and dacite at geologically relevant temperatures of 1473–1773 K (Boulliung and Wood 2022), we turn our attention back to sulfide capacity. The approach taken by previous authors has almost exclusively been to determine sulfur concentration (or sulfide capacity) at fixed temperature for a limited range of compositions. These restrictions apply to the data of Buchanan and Nolan (1979) at 1473 K, Haughton et al. (1974) for basaltic compositions, Nash et al. (2019) at 1573 K and O'Neill and Mavrogenes (2002) at 1673 K. It would, in principle, be perfectly reasonable to draw these disparate data together to make a comprehensive model as done by O'Neill (2021). Our approach, however, was to explore the effect of temperature, in a single study, on the sulfide capacities of a number of melts at atmospheric pressure. We opted to determine sulfide capacities of 13 of the same melts for which we recently determined sulfate capacities (Boulliung and Wood 2022) and over the same temperature range of 1473–1773 K (with 50 K increments). From these data, a new equation was developed to represent sulfide capacity in silicate melts at 1 atm, as functions of their composition and the temperature. By combining the measured sulfide capacity with sulfate capacity data from Boulliung and Wood (2022), we provide new constraints on the temperature and melt composition effects on the sulfate/sulfide crossover, on the fO_2 dependence of degassing species and on the effect of sulfur degassing on magma oxidation state.

Experimental and analytical methods

Starting materials

In order to study the effects of melt composition and temperature on sulfide solubility in silicate melts at low pressure, we used a similar experimental method to that of Boulliung and Wood (2022). In this previous study, we determined sulfur concentrations and sulfate capacities in 14 silicate melts under strongly oxidizing conditions at 1 atmosphere pressure and 1473–1773 K. Here, we were aiming to determine sulfide capacities of 13 of the same melt compositions (Table 1) under identical pressure–temperature conditions. The 14th composition, rhyolite, is excluded because we were unable to obtain homogeneous melts in experiments of 8 h duration. The starting materials cover a wide range of compositions, from basanite to an andesite–dacite transitional composition ("Andac"). Three iron-free CMAS compositions were also synthesized (CMAS1, CMAS2 and CMAS3) in order to determine the sulfide capacity in iron-free silicate melts. A wide range

of FeO contents (from 0 to 16.9 wt%) was also employed to constrain the well-known positive effect of iron content on sulfide solubility (e.g., O'Neill and Mavrogenes 2002; Namur et al. 2016; Smythe et al. 2017).

Experimental conditions

The equilibration experiments were performed in a Gero vertical furnace (HTRV 70-250/18) at atmospheric pressure in a controlled CO–CO_2–SO_2 atmosphere. Nash et al. (2019) showed that for experiments at 1 atm and 1573 K the $S^{6+}/\Sigma S$ of silicate melts is < 0.1 for $fO_2 <$ FMQ. In order, therefore to stabilize sulfur entirely as sulfide in the silicate melt, $fO_2 > 1$ log unit below FMQ was imposed (Table 2). The gas mix flux in the vertical furnace was controlled by Tylan mass flow controllers and was in most cases maintained at 250 cm³ min⁻¹ equivalent to a linear velocity of 0.23 cm/s. Gas flow in experiments at 1573 K was 295 cm³ min⁻¹ in order to reproduce the conditions used by Nash et al. (2019). The different fO_2 and fS_2 represented in Table 2 were calculated from thermodynamic data for C–S and O-bearing species (Chase 1985) following the procedure of White et al.

Table 1 Major oxide compositions of the starting materials determined by electron microprobe analysis before sulfide equilibrium experiments

Composition	SiO_2	Al_2O_3	MgO	CaO	FeO	TiO_2	K_2O	Na_2O	MnO	P_2O_5	Total	n
T-Basalt	47.0 (1)	16.4 (1)	4.3 (1)	9.4 (1)	10.3 (2)	3.33 (4)	1.87 (3)	4.68 (4)	0.21 (2)	1.24	98.7	10
Lunar Basalt	42.3 (2)	11.9 (1)	7.5 (1)	9.6 (1)	16.9 (1)	8.34 (6)	0.20 (3)	0.88 (2)	0.58 (2)	–	98.2	10
NIB	49.6 (1)	14.6 (1)	8.7 (1)	12.4 (1)	9.0 (1)	0.92 (2)	0.21 (6)	2.25 (6)	0.17 (5)	0.30	98.2	10
Nephelinite	41.7 (1)	14.2 (1)	8.0 (1)	13.9 (1)	9.9 (1)	2.68 (1)	3.21 (3)	3.95 (4)	2.45 (2)	–	99.9	8
Andac	61.6 (9)	19.0 (9)	2.0 (2)	4.1 (3)	4.9 (3)	1.04 (4)	4.60 (9)	0.87 (3)	b.d.l	–	98.1	8
B-A	53.9 (5)	14.6 (2)	9.4 (2)	9.9 (2)	6.4 (1)	0.61 (1)	1.34 (5)	2.79 (6)	b.d.l	–	99.0	8
Andesite	61.1 (6)	18.0 (2)	3.5 (1)	6.9 (2)	3.9 (1)	0.61 (1)	1.19 (4)	4.07 (6)	b.d.l		99.2	10
Basanite	43.8 (1)	10.9 (1)	13.1 (1)	9.4 (1)	11.5 (1)	2.28 (3)	1.89 (2)	3.94 (4)	0.18 (5)	1.45	98.4	10
T-Phonolite	53.3 (9)	22.9 (9)	1.9 (1)	4.8 (3)	4.4 (1)	1.50 (6)	3.64 (9)	7.77 (9)	b.d.l	–	100.4	8
SLC	39.9 (1)	10.9 (1)	15.4 (1)	17.3 (1)	14.4 (1)	b.d.l	b.d.l	0.13 (3)	b.d.l	–	98.0	8
CMAS1	48.4 (1)	16.8 (2)	12.4 (1)	22.3 (1)	b.d.l	b.d.l	b.d.l	b.d.l	b.d.l	–	100.1	10
CMAS2	45.5 (1)	18.7 (1)	17.4 (1)	18.4 (1)	b.d.l	b.d.l	b.d.l	b.d.l	b.d.l	–	100.1	10
CMAS3	50.4 (1)	15.6 (1)	14.5 (1)	19.6 (1)	b.d.l	b.d.l	b.d.l	b.d.l	b.d.l	–	100.2	10

The starting materials are the same as in the Boulliung and Wood (2022) sulfate solubility study. Numbers in parentheses represent 1σ uncertainties on the last digit. "b.d.l." corresponds to "below detection limit"

Table 2 Run conditions, gas mixtures and durations of sulfide equilibration experiments in atmosphere controlled furnace

Temperature (K)	CO	CO_2	SO_2	log fO_2	FMQ	log fS_2	t (h)
1473	110	70	70	− 9.40	− 1.1	− 1.05	8
1523	103	87	60	− 8.98	− 1.24	− 1.15	8
1573	148	99	48	− 8.98	− 1.76	− 1.21	8
1623	175	30	45	− 8.99	− 2.26	− 1.08	8
1673	200	12.5	37.5	− 8.97	− 2.71	− 1.15	8
1723	208	22	20	− 8.99	− 3.16	− 1.44	6
1773	219	19	12	− 8.94	− 3.52	− 1.61	3

(1958). The gas mixture flow was maintained for at least 10 min prior to each experiment in order to approach the desired fO_2 and fS_2 before beginning equilibration (Boulliung et al. 2020). Between 5 and 10 mg of each starting composition were suspended in the furnace on a 0.25-mm-diameter rhenium wire loop and stuck to the loop using polyvinyl alcohol solution. Up to 7 experimental charges were hung at the same time on a platinum chandelier suspended from a silica rod.

In order to determine the effect of temperature on sulfate capacity (Boulliung and Wood 2022), we used 7 different temperatures ranging from 1473 to 1773 K (in 50 K increments; Table 2). O'Neill and Mavrogenes (2002) performed S equilibration experiments using ~ 50 mg of starting material and determined that steady state was reached, respectively, after ~ 8 and 4 h in an Fe-free and Fe-bearing composition at 1673 K. Since we used only about 1/5 as much starting material as in O'Neill and Mavrogenes (2002), we anticipated much shorter equilibration times than they observed. The time required for gas–melt equilibration was therefore determined by running Fe-free and Fe-bearing compositions (CMAS1 and basanite, respectively) from 1 to 8 h at 1673 K. The results show that constant S contents for both of these compositions were already reached after ~ 2 h (see supplementary information for more details). Given these results and to ensure a close approach to equilibrium, experiments at 1473 to 1673 K lasted 8 h. For the experiments at higher temperatures, 1723 and 1773 K, 6 and 3 h were used, respectively (Table 2). The samples were quenched in the reduced S-bearing atmosphere, by rapidly pulling the chandelier to the cold area at the top of the vertical furnace. After the experiment, the quenched glasses were mounted in epoxy and polished. The samples were carbon coated for electron microprobe analysis.

Analyses

The major element compositions and the S contents of the glasses were determined by electron microprobe analysis at the University of Oxford, Department of Earth Sciences, using a Cameca SX-Five-FE operating at 45 nA and 15 kV with a spot size of 10 μm. The standards used for the silicate glass compositions were natural albite (Si, Al, Na), andradite (Ca, Fe), sanidine (K) and pyrite (reduced S). A secondary standard, L17 basaltic glass (1320 ppm S; Nash et al. 2019; Boulliung and Wood 2022), was used to verify the calibration and was re-analyzed during each probe session. Counting times were a minimum of 30 s peak and 15 s background for all elements except for Na and K, for which 20 s peak and 10 s background were used to reduce the element migration rates induced by the beam. For sulfur, 80 s peak and 40 s background were used to obtain a

detection limit of ~ 60 ppm. Between 10 and 30 points were analyzed on each sample in order to verify that the glass was homogeneous.

Results

Sulfide capacity as function of temperature and melt composition

The melt compositions and sulfide capacities of each sample are reported in Supplementary Table. All partially crystallized experimental products showing significant differences from the starting composition have been excluded. Apart from the presence of crystals in some products, the only significant compositional changes were the occasional losses and gains of small amounts of alkali elements (i.e., Na_2O and K_2O; Supplementary Table). This phenomenon is already well known (e.g., O'Neill 2005).

Sulfur abundances and sulfide capacities (with S in wt%), obtained on the glass products, are summarized in Supplementary Table. The sulfide capacity was calculated following Fincham and Richardson (1954), Eq. (2). Uncertainties in log C_{S2-} were calculated using the standard deviations of the measured S contents combined with the estimated 0.1 log unit uncertainties in fO_2 and fS_2. The results show an increase in sulfide capacity with temperature, the opposite temperature dependence from that observed for sulfate capacity (Boulliung and Wood 2022; Fig. 1a). In terms of solubility, the S content of the Icelandic basalt (NIB) increases from 760 ± 25 to 2433 ± 39 ppm as the temperature increases from 1473 (FMQ – 1.1 and log $fS_2 = -1.05$) to 1673 K (FMQ – 2.71 and log $fS_2 = -1.15$). Similar temperature effects are observed for all melt compositions studied (Fig. 1a).

In addition to a temperature effect, Fig. 1a shows that melt composition has a profound effect on sulfide capacity. For example, at 1473 K, the logarithm of the sulfide capacity (log C_{S6+}) ranges from – 5.90 (phonolite) to – 4.94 (nephelinite), an increase correlated with increasing FeO and CaO contents of the melt. As anticipated, however, and as observed in earlier studies (e.g., O'Neill and Mavrogenes 2002), FeO content of the melt is the major controlling factor (Fig. 1b). At 1573 K, for example, the sulfide capacity of the melt increases from – 5.55 to – 4.33, as FeO concentration increases from 0 to 16.4 wt% (Fig. 1b).

A quantitative description of sulfide capacity as a function of temperature and composition

We used the experimental results given in Supplementary Table to obtain a best-fit equation, which incorporates the significant compositional and temperature effects on sulfide
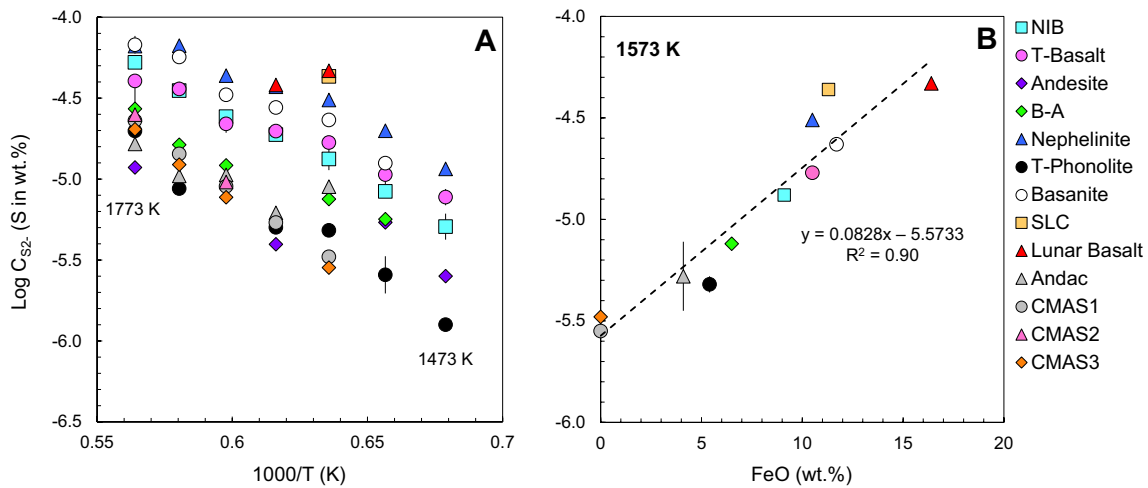
Fig. 1 Temperature (**A**) and FeO content (**B**) effect on sulfide capacity for the different melt compositions. In **A,** all compositions and temperatures (ranging from 1473 to 1773 K) are shown. In **B,** only the data obtained for the experiments at 1573 K are shown. The iron content is given as total Fe as FeO

capacity. We adopted the form of the equation derived by O'Neill and Mavrogenes ([2002](#)). These authors showed that at fixed temperature and pressure the sulfide capacity log C_{S2-} should have the following form:

$$\log C_{S^{2-}} = A_0 + \sum_M X_M A_M \tag{5}$$

In Eq. ([5](#)), X_M refers to the oxide mole fraction on a single-oxygen basis ($Si_{0.5}O$, $Al_{0.67}O$, MgO, CaO, etc.) and A_0 is a constant. The A_M terms are related to the differences between the free energies of formation of the oxide and sulfide components of the individual cations, i.e.,

$(G^0_{CaO} - G^0_{CaS})$; $(G^0_{FeO} - G^0_{FeS})$ and so on. There are several assumptions in the model, notably that the cations and anions mix with ideal entropy on the individual sublattices, but for our purposes this provides a form of equation with some theoretical basis. Because we have data over a temperature range from 1473 to 1773 K and log C_{S2-} has the form of an equilibrium constant, the temperature dependence should be represented by a term in reciprocal temperature. In order not to over-fit the data, we opted to use stepwise linear regression to an equation of the form of Eq. ([5](#)) to which a $1/T$ term was added and in which the A_M terms were divided by T to ensure that they approach zero in the limit of infinite
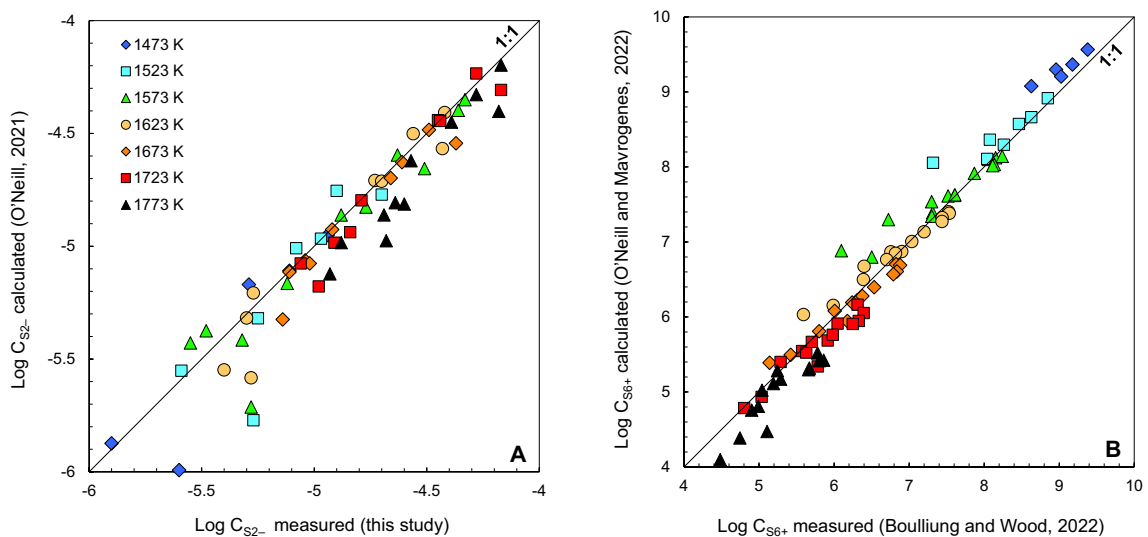

Fig. 2 **A** Sulfide capacities measured (this study) as a function of log C_{S2-} calculated using the O'Neill ([2021](#)) model. **B** Measured sulfate capacities (Boulliung and Wood [2022](#)) plotted against log C_{S6+} calculated using the O'Neill and Mavrogenes ([2022](#)) equation
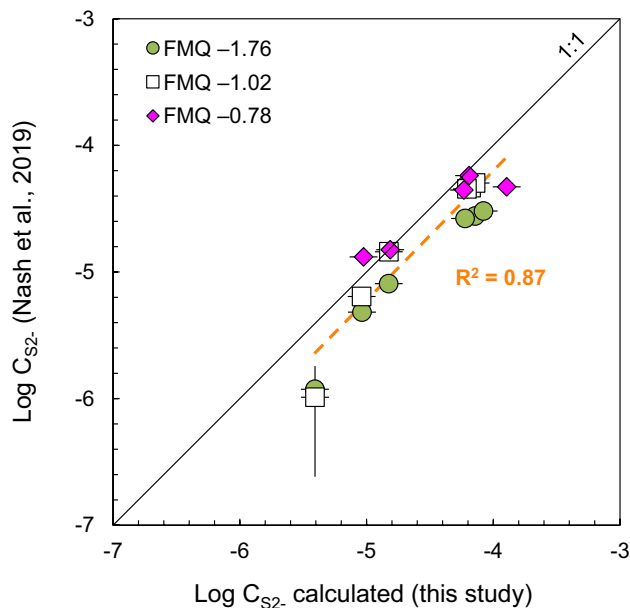
Fig. 3 Comparison between the measured log C_{S2-} from Nash et al. (2019) and the log C_{S2-} calculated using our fit Eq. (7) on the final glass compositions. The data from Nash et al. (2019) are for 6 different melt compositions (from Fe-rich basalt to dacite) and three different redox conditions (i.e., FMQ – 0.78, – 1.02 and FMQ – 1.76). Under these conditions, S is mostly incorporated as sulfide with a $S^{6+}/\Sigma S$ ratio (XANES) < 0.03

temperature. We used the SPSS statistical package to perform the stepwise regression in which terms were added sequentially and tested for significance at each step. Terms which did not pass the F test at $\alpha = 0.05$ were excluded, resulting in the following fit equation (1 standard error in brackets) (6):

$$\log C_{S^{2-}} = 0.338(0.219) + \big(24328(1149)X_{FeO} \\ + 5411(627)X_{CaO} + 15872(5294)X_{MnO} \\ - 9697(369)\big)/T$$ (6)

The standard error of the fit is 0.1, and the R^2 is 0.95. In deriving Eq. 6, we calculated X_{FeO} from the total Fe content of the melt at the temperature and fO_2 of the experiment using the Kress and Carmichael model (Kress and Carmichael 1991). X_{FeO} thus refers to the actual FeO content of the glass, not the total Fe content.

Discussion

Comparison with previous studies

There have been a number of earlier studies of sulfide capacity in natural silicate melts, and these provide us with reference points with which to check and verify our

data. O'Neill and Mavrogenes (2002) determined log C_{S2-} at 1 atm pressure and 1673 K for 19 compositions in the SiO_2-Al_2O_3-MgO-CaO-TiO_2-FeO system and 150 additional compositions with various proportions of Na and K. Since O'Neill and Mavrogenes (2002) obtained data on a wide range of compositions, we combined their results at 1673 K with ours from 1273 to 1773 K and refit the combined dataset using the same stepwise approach as before. In order to impose consistency between the two experimental studies, we only added data of O'Neill and Mavrogenes (2002) where the experiment duration was at least 8 h. This approach led to the following equation (1 standard error in brackets) (7):

$$\log C_{S^{2-}} = 0.225(0.190) + \big(25237(784)X_{FeO} + 5214(838)X_{CaO} \\ + 12705(4420)X_{MnO} + 19829(7139)X_{K_2O} \\ - 1109(337)X_{Si_{0.5}O} - 8879(408)\big)/T$$ (7)

The standard error of the fit is 0.09, and R^2 is 0.96, virtually identical to the results for our data alone. Furthermore, it can be seen that the major terms in CaO and $1/T$ are virtually identical in both fit equations and that the FeO term is very similar. Unlike O'Neill and Mavrogenes (2002), however, we did not find the $X_{FeO}X_{Ti0.5O}$ term to be significant at the $\alpha = 0.05$ level.

O'Neill (2021) extended the O'Neill and Mavrogenes (2002) study by adding literature and unpublished data at different temperatures, predominantly 1473 K, to derive a temperature dependence of sulfide capacity. In Fig. 2a, we compare our measured results for C_{S2-} with the O'Neill equation for sulfide capacity. As can be seen, agreement is generally very good albeit with a small shift to lower than measured sulfide capacities in the O'Neill equation. This discrepancy could have arisen from the need for O'Neill (2021) to combine, in his fit equation, data from different laboratories with the potential for systematic errors. In Fig. 2b, we show, for completeness, a comparison of our results for sulfate capacity (Boulliung and Wood 2022) with the model derived by O'Neill and Mavrogenes (2022). Agreement is again encouragingly good with the only possible difference being a small difference in the measured (Boulliung and Wood 2022) and modeled (O'Neill and Mavrogenes 2022) temperature dependence of C_{S6+}.

Nash et al. (2019) performed S-bearing experiments at 1573 K and 1 atm for a wide range of melt compositions (from Fe-rich Martian basalt to dacite) under redox conditions spanning the range from essentially 100% sulfide to 0% sulfide. They determined the sulfur speciation in their final run products by X-ray Absorption Near-Edge Spectroscopy (XANES) and by a new method based on measurement of the S content of the melt at known fO_2/fS_2 (Nash et al. 2019). In order to compare with our results, we calculated sulfide capacities from the S concentrations of Nash et al. (2019) using only those data for which $S^{6+}/\Sigma S$ was determined to

be less than 0.03 (fO$_2$ ≤ FMQ – 0.78; Fig. 3). These data were then compared with our fit Eq. (7) in Fig. 3. Agreement between our model and the Nash et al. (2019) data is generally excellent. The exceptions are 2 data points on a dacite at low $C_{S^{2-}}$. The S contents in all the Nash et al. (2019) experimental products were measured by secondary-ion mass spectrometry (SIMS), however, and it is likely that the observed differences from our model, based on electron microprobe analyses (Supplementary Table), are largely due to matrix effects on secondary ion yields in the SIMS analysis. The SIMS analyses of Nash et al. (2019) used the ratio of ^{32}S to ^{18}O counts with an iron-rich Martian basalt (JFR) as the primary standard and a terrestrial basalt (L17) as the secondary standard. Given that ion yields are compositionally dependent, it is likely that the small differences between standards containing less than 50% SiO$_2$ and the dacite with up to 64 wt.% SiO$_2$ are due to slightly different ion yields.

Implications for the crossover from S^{2-} to S^{6+} in silicate melts

The fO$_2$ conditions under which S^{2-} becomes unstable with respect to S^{6+} are of considerable geological interest. Matjuschkin et al. (2016), based on experiments at 0.5–1.5 GPa and 1173–1223 K, proposed that pressure has a strong effect on the relative fO$_2$ at which the S^{2-}–S^{6+} transition occurs. They suggested that the stability field of S^{2-} shifts from just above the Ni-NiO (NNO) buffer at 0.2 GPa to about 2 log fO$_2$ units above the buffer at 1.5 GPa. If correct, this would imply that sulfides are very stable in the lower crust leading to early sulfide precipitation in thick continental arcs and lack of Cu enrichment in the evolving melts (Rezeau and Jagoutz 2020). Such early sulfide precipitation, which could only be suppressed at very high fO$_2$, would profoundly impact the development of copper porphyry deposits. The contrasting view, put forward by Nash et al. (2019), is that the effects observed experimentally by Matjuschkin et al. (2016) are entirely due to the temperature differences between their experiments and those of earlier workers who performed experiments at higher temperatures. In support of this hypothesis, Nash et al. (2019) presented estimated thermodynamic data for the model homogeneous equilibrium in the melt phase (Eq. 8):

$$FeS + 8FeO_{1.5} = 8FeO + FeSO_4 \tag{8}$$

The data, which were based on the properties of pure solids and not measured in any melt, suggest that the equilibrium moves strongly to the left as temperature is reduced, stabilizing sulfide at the expense of sulfate in the melt. If correct, this model indicates that pressure effects are minor

and that sulfide is not stabilized at high fO$_2$ in the lower crust. Relatively oxidized melts would instead tend to precipitate sulfide during cooling at any level in the crust.

We will now use our data to investigate the 2 end-member hypotheses for the observed shift in S^{2-}-S^{6+} transition interval with changing physical conditions. The calculation requires that we adopt the data of Boulliung and Wood (2022) on the sulfate capacities of many of the same melts as those used in the current study. For convenience, the sulfate capacity data of Boulliung and Wood (2022) were refit on a single-oxygen basis so that the sulfate capacity equation mirrors Eq. (7) for sulfide capacity. We used the same approach of stepwise multiple linear regression with only those parameters passing the F test at the $\alpha = 0.05$ level being accepted. This led to (1 standard error in brackets):

$$\begin{aligned}
\log C_{S^{6+}} = &-12.948(0.278) \\
&+ \big(28649(4040)X_{Na_2O} + 15602(1645)X_{CaO} \\
&+ 9496(1279)X_{MgO} + 16016(7128)X_{MnO} \\
&+ 4194(1163)X_{Al_{0.67}O} + 29244(493)\big)/T
\end{aligned} \tag{9}$$

The standard error of the fit is 0.14, and R^2 is 0.988.

Equations (7) and (9) for sulfide and sulfate capacity, respectively, were used together with Eqs. (2) and (4) to determine the S^{6+}/ΣS ratio (S^{6+}/ΣS = S^{6+}/(S^{6+} + S^{2-}) as a

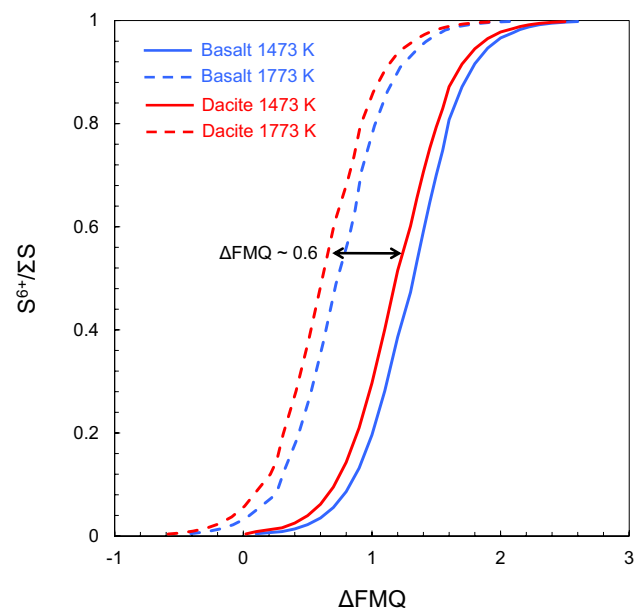**Fig. 4** The ratio of S^{6+}/(S^{6+} + S^{2-}) as a function of fO$_2$ (relative to the FMQ buffer; Frost 1991) at 1 bar for average basalt and average dacite compositions of Carmichael et al. (1974) at the upper (1773 K) and lower (1473 K) temperature limits of our data

function of temperature, composition and fO_2. A spreadsheet to enable calculation of sulfide and sulfate capacity at fixed temperature and composition is provided in supplementary information.

Calculated temperature and pressure effects

We begin by considering the temperature effect on the fO_2 of the S^{2-} to S^{6+} transition in the temperature interval (1473–1773 K) where we have data for a wide range of rock compositions. Figure 4 shows the log fO_2 interval obtained for average basalt and average dacite compositions (Carmichael et al. 1974). As can be seen, there is in both cases a positive shift of about 0.6 log fO_2 units relative to the FMQ buffer curve as temperature is decreased from 1773 to 1473 K. For comparison, the temperature effect suggested by Nash et al. (2019) corresponds to a positive shift of 1.15 log fO_2 units relative to FMQ for the basalt shown in Fig. 4. O'Neill (2021) criticized the Nash model and proposed 8 possible equations all of which would give much smaller temperature effects. If we take as an example his preferred "weighted average," however, the O'Neill and Mavrogenes (2022) model gives a shift of only + 0.11 log fO_2 units relative to FMQ as temperature is reduced from 1773 to 1473 K. This is clearly much smaller than the observed shift.

Although experimental data on the effect of pressure on the S^{2-} to S^{6+} transition are limited and disparate, the measured volumes of metal oxides, sulfides and sulfates can probably be used to make a rough estimate. This follows the observation of Thomas and Wood (2021) that the effect of pressure on the replacement of O^{2-} by Cl_2^{2-} in melts could be modeled almost exactly by the volume difference between $CaCl_2$ and CaO. Therefore, given the correlation between sulfate capacity and CaO (Boulliung and Wood 2022) and between sulfide capacity and FeO (this study), we modeled the effect of pressure on sulfate capacity by the volume difference between $CaSO_4$ and CaO ($+29.2$ cm^3 mol^{-1}), and the pressure effect on sulfide capacity by the volume difference between FeS and FeO ($+6.2$ cm^3 mol^{-1}). The difference between these two corresponds to ΔV for the reaction:

$$FeS + CaO + 2O_2(gas) = FeO + CaSO_4$$

$$\Delta V(solids) = 23 \text{ cm}^3\text{mol}^{-1}$$
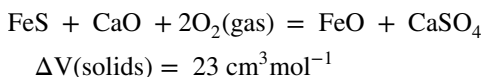
Because this volume change involves 2 oxygen molecules, it is divided by 2 to yield the pressure effect on fO_2. The result (11.5 cm^3 mol^{-1}) is divided by 10 to convert to J bar^{-1}, by 2.303 to convert to base10 logarithms and by 8.314 (gas constant R) to yield:

$$\log\left(f_{O2}^{Pbar}\right) = \log\left(f_{O2}^{1bar}\right) + \frac{0.06(P-1)}{T} \qquad (10)$$

In Eq. (10), pressure is in bars. Thus, the absolute fO_2 of the S^{2-}–S^{6+} crossover increases by 0.4 log units on increasing pressure from 0 to 1 GPa at 1573 K. The fO_2 values of all of the oxygen buffers also increase with pressure, however, so that there is a much smaller shift of the transition to higher fO_2 relative to the Ni-NiO buffer used by Matjuschkin et al. (2016). This would correspond only to ~0.1 log fO_2 units at 1 GPa. Relative to FMQ, the pressure effect on fO_2 should actually be negative rather than positive. We conclude that, as suggested by Nash et al. (2019), the effect of temperature on the relative fO_2 of the S^{2-}-S^{6+} transition dominates over that of pressure, albeit with a smaller temperature dependence than that proposed by these authors.

Comparison with hydrous experiments at lower temperatures

Extrapolation of our results to temperatures below 1473 K depends on the temperature dependences of sulfide and sulfate capacities being accurately reproduced by fit equations in the range 1473–1773 K. Fortunately, there are data available from lower temperatures, but the experimentally derived glasses contain ~4–7 wt% H_2O in addition to S and the other major oxides. As a starting point, we will ignore H_2O and recalculate the product melts on an anhydrous basis.

Jugo et al. (2010) used XANES spectroscopy to determine $S^{6+}/\Sigma S$ for basaltic melts quenched from 1323 K, 2000 bars and oxygen fugacities from FMQ − 1.4 log fO_2 units to FMQ + 2.7. Botcharnikov et al. (2011) performed similar measurements on the same experimentally produced basalts and also on andesitic melts generated at 1323 K, 2000 bars and from FMQ − 0.40 to FMQ + 3.30. For the $S^{6+}/\Sigma S$ calculations, the reference FMQ buffer equilibrium refers to the Frost (1991) equation. When
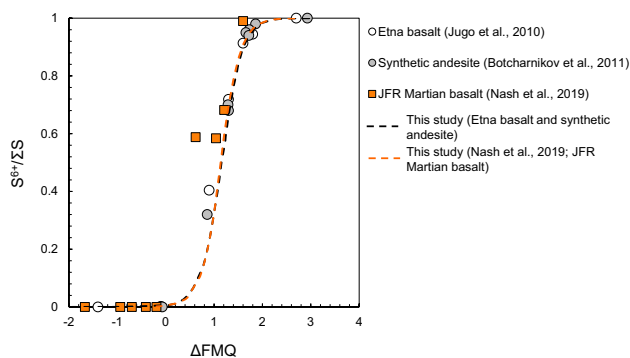

Fig. 5 Observed $S^{6+}/\Sigma S$ from experimental run products compared to calculated values from our sulfide and sulfate capacities (dashed lines). The $S^{6+}/\Sigma S$ data from Jugo et al. (2010) and Botcharnikov et al. (2011) were obtained by XANES on melts equilibrated at 1323 K and 2000 bars. The sulfur speciation data of Nash et al. (2019) were obtained by analysis of melts equilibrated at 1573 K and 1 bar

compared with the experimentally produced glasses, Eqs. (7) and (9) slightly overestimate the fO_2 of the S^{2-} to S^{6+} transition, by about 0.25 log fO_2 units, a value within the combined experimental uncertainties. On inspection of our data on sulfate capacity, however, we noted a slight curvature on a plot of log C_{S6+} versus $1/T$, such that log C_{S6+} fits better as a function of $1/T^2$ than to $1/T$ in the narrow temperature range 1473–1773 K. In practice, this implies a large heat capacity difference between the products and reactants of reaction (3), which manifests itself as a term in log T in the equation for sulfate capacity. Adopting this approach for our sulfate capacity data and performing stepwise linear regression yielded an equation with a standard error of 0.135 in log C_{S6+} and R^2 of 0.99:

$$
\begin{aligned}
log\,C_{S6+} = & -213.65(89.95) \\
& + \big(25696(4131)X_{Na2O} + 15076(1616)X_{CaO} \\
& + 9543(1243)X_{MgO} + 16158(6932)X_{MnO} \\
& + 4316(1132)X_{Al_{0.67}O} + 68254(16907)\big)/T \\
& + 55.03(23.84)log\,T
\end{aligned} \tag{11}
$$

Use of this equation reproduces the results of Nash et al. (2019) at 1573 K and also those of Jugo et al. (2010) and Botcharnikov et al. (2011) within 0.1 log fO_2 units, or better than the experimental uncertainty (Fig. 5). Note that the near-coincidence of the crossover for Martian basalt at 1573 K and terrestrial andesite at 1323 K is due to two competing effects. The higher FeO content of the Martian

basalt shifts the curve to the right, while its higher temperature shifts it to the left. The result is near-coincidence for the two sets of experiments at different compositions and temperatures.

Although Eq. (11) captures the temperature dependence of sulfate capacity in our experimental temperature range very well and appears to allow limited extrapolation to lower temperatures, we advise caution in its use. This is because the heat capacity difference implied by the log T term is unreasonably large. Furthermore, the lower temperature data used here come from hydrous rather than anhydrous experiments.

As indicated above, the sulfide and sulfate capacities of a melt may reasonably be expected to depend on its water content (e.g., Moretti and Ottonello 2005; Xu and Li 2021; Boulliung and Wood 2022). Depending on the amount of water and the melt composition, the S^{2-} and S^{6+} capacities may either increase or decrease (Moretti and Ottonello 2005). Experiments to date (Jugo et al. 2010; Botcharnikov et al. 2011) do not, however, enable us to determine the effects of the water on either sulfate or sulfide capacities. We are left simply with the observation that there is very good agreement between the measured $S^{6+}/\Sigma S$ (Fig. 5) for these hydrous experiments and the oxidation ratio predicted from our anhydrous experiments (Fig. 5). O'Neill and Mavrogenes (2022) obtained similar results to us and suggested, therefore, that the effects of water on C_{S2-} and C_{S6+} (C^H_{S2-} and C^H_{S6+}) are similar.
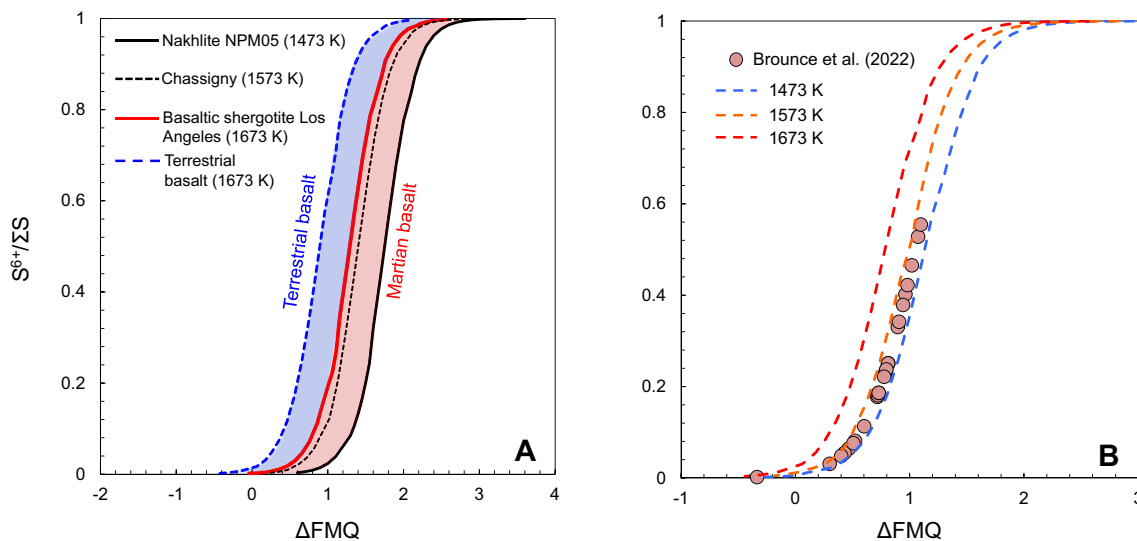

Fig. 6 A Sulfur speciation for terrestrial basalt and for Martian basalts based on SNC meteorites and parent magma composition estimates. The blue area corresponds to the $S^{6+}/(S^{6+}+S^{2-})$ (or $S^{6+}/\Sigma S$) range for average terrestrial basaltic composition (Carmichael et al. 1974) at temperatures between 1473 and 1673 K. The red area includes all the Martian basaltic compositions for temperatures

between 1423 and 1673 K (see text). **B** Comparison of $S^{6+}/\Sigma S$ calculated from sulfide and sulfate capacities at 1473–1673 K with values measured in glass mesostasis from Nakhla meteorite (Brounce et al. 2022). Brounce et al. (2022) estimated log fO_2 using calibration of Jugo et al. (2010)

The redox state of S in Martian magmas

Our simulation of the S^{2-} to S^{6+} crossover for Fe-rich Martian basalt JFR (17.4 wt% FeO) at 1573 K is in very good agreement with the Nash et al. (2019) data (Fig. 5). As an illustration of the major compositional effect on $S^{6+}/\Sigma S$, we compare oxidation state as a function of fO_2 for terrestrial basalt and Martian basalt in Fig. 6a. For the crossover simulation (Fig. 6a), we used three different Martian basaltic compositions: (i) the parent magma estimation for NPM05 nakhlite (Sautter et al. 2012); (ii) the bulk composition of Los Angeles basaltic shergottite (Rubin et al. 2000); and (iii) the parent liquid for Chassigny A* Johnson estimated using PETROLOG calculations (Hewins et al. 2020). Two different temperatures (i.e., 1473 and 1673 K) were used to determine the effect of T on the different $S^{6+}/\Sigma S$ ratios. The simulation in Fig. 6a shows that Martian basaltic compositions require more oxidizing conditions to stabilize sulfate than terrestrial basalts. This is due to the stabilizing effect of their high FeO contents (Eq. 7) on reduced S^{2-} dissolved in the melt.

The oxygen fugacities determined by oxybarometry for Martian basalts are generally below FMQ and well within the range of S^{2-} stability, i.e., $fO_2 \leq$ FMQ −1 (Floran et al. 1978; Herd et al. 2001, 2002; Gaillard and Scaillet 2009; Hewins et al. 2020). There is, however, evidence for more oxidizing conditions during magmatic differentiation. For example, based on the V-in-olivine oxybarometry method (Canil 1997), Nicklas et al. (2021) suggested that shergottites and chassignites reach relatively oxidized conditions during their evolution. During the early phases of crystallization of shergottites, they find fO_2 values ranging from FMQ −3.72 log fO_2 units to FMQ −0.21. In the later magmatic stages, however, fO_2 appeared to reach FMQ + 2.2 log units. Similarly, Wang et al. (2021) found redox conditions reaching FMQ + 1.6 log units in Northwest Africa nakhlite. Furthermore, the presence of magnetite and maghemite in Martian meteorite (NWA 7034; Agee et al. 2013) and the high S contents observed in surface rocks (~ 2.5 wt% in Gusev crater soil; McSween 2015) are consistent with redox conditions reaching $fO_2 \sim$ FMQ + 2 to FMQ + 3 (Tuff et al. 2013).

Brounce et al. (2022) used sulfur-XANES to determine the oxidation state of sulfur in apatites and associated glassy mesostasis from the Nakhla meteorite. They calculated apparent fO_2 of the glasses using the calibration of Jugo et al. (2010). In Fig. 6b, we compare S oxidation state in average Nakhla mesostasis calculated from our results with values obtained by Brounce et al. (2022) using the Jugo et al. (2010) calibration. As can be seen, agreement is excellent at temperatures just above 1473 K, temperatures which, given the accumulated uncertainties in oxidation state data and 2 different experimental calibrations, is very

gratifying. Brounce et al. attribute the relatively high oxygen fugacities recorded by these interstitial glasses and related apatites as due to late stage degassing of a Cl-bearing volatile phase.

Comparison with terrestrial basaltic glasses

Brounce et al. (2017) used XANES spectroscopy to determine the Fe^{3+}/Fe^{2+} and S^{6+}/S^{2-} ratios of basaltic glasses from Mauna Kea, Hawaii. They observed negative correlations between glass sulfur content (1480–350 ppm) and $S^{6+}/(S^{6+} + S^{2-})$ and $Fe^{3+}/(Fe^{3+} + Fe^{2+})$ in the quenched melts. These observations were interpreted as reflecting reduction of the melt during degassing of a C-O–H-S volatile phase at near-liquidus temperatures of ~ 1473 K. Nash et al. (2019) reinterpreted the glass data using an estimated temperature dependence of the equilibrium constant for exchange of electrons between Fe^{2+} and S^{6+}. These authors then used the glass data to calculate an average apparent temperature of Fe-S equilibrium of 1266 K with a standard deviation of 30°. The result implies that Fe-S electronic equilibrium is quenched-in close to, or below the basalt solidus rather than at the eruption temperature. We have shown earlier, however, that the Nash et al. experimental data at 1573 K are consistent with our results at this temperature but also that these authors overestimated the temperature effect on the Fe-S electron exchange equilibrium. We can further test the latter conclusion by applying our results for sulfate and sulfide capacity to the Brounce et al. (2017) glass data.

We used the glass major element compositions of Brounce et al. (2017) to calculate sulfide and sulfate capacities using Eqs. (7) and (11), respectively, at an initial estimated temperature T^0. We then used the measured $Fe^{3+}/(Fe^{3+} + Fe^{2+})$ to calculate, at this temperature, fO_2 from Kress and Carmichael (1991) and $S^{6+}/(S^{6+} + S^{2-})$ from Eqs. (2) and (4) given our sulfide and sulfate capacities. We then compared the calculated $S^{6+}/(S^{6+} + S^{2-})$ with those measured by Brounce et al. and adjusted temperature until observed and calculated values were in agreement. This resulted in an average temperature of 1479 K with a standard deviation of 46° (Fig. 7). The result is in excellent agreement with Brounce et al.'s assumption of equilibration close to 1473 K and confirms that the temperature dependence of S oxidation state proposed by Nash et al. (2019) is an overestimate.

Implications for S degassing during magma ascent

In order to simulate S degassing during magma ascent, we used a similar approach to that of Boulliung and Wood (2022). This began with an assumed fO_2, temperature (1473 K) and sulfur content of the melt at an initial pressure
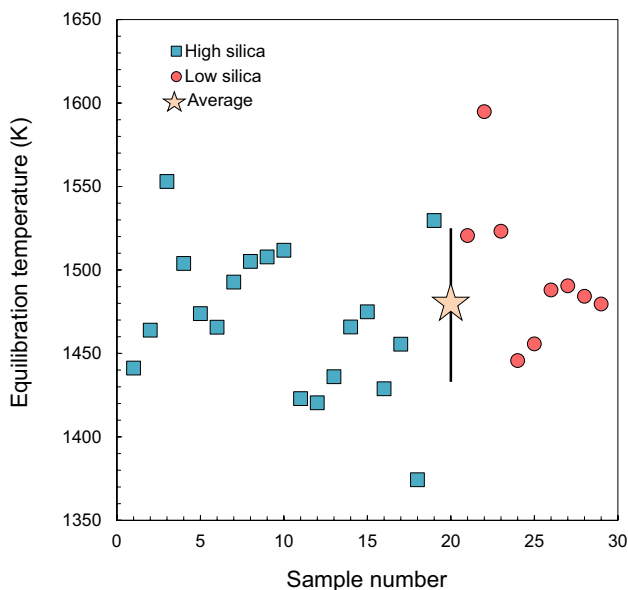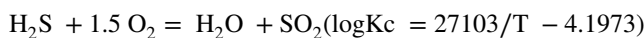
Fig. 7 Calculated temperatures of Fe^{3+}/Fe^{2+} equilibrium with S^{6+}/S^{2-} obtained from the Mauna Kea glass oxidation state data of Brounce et al. (2017). Calculated sulfur oxidation state from this study and Fe^{3+}/Fe^{2+} from Kress and Carmichael (1991). Error bar is one standard deviation of the average. The sample numbers were allocated arbitrarily in order to separate the high and low silica compositions. Note that equilibrium temperatures are ~200° higher than those proposed by Nash et al. (2019)

of 250 MPa (Fig. 8). The fO_2 was used to calculate the Fe^{3+}/Fe^{2+} ratio of the melt using the equation of Kress and Carmichael (1991) and the sulfate and sulfide capacities of the

melt calculated from Eqs. (7) and (9) adjusted to the initial pressure using Eq. (12):

$$log_{C_{S^{6+}}}(P,T) = log_{C_{S^{6+}}}(1bar, T) + \frac{(P-1)\Delta V}{2.303RT} \quad (12)$$

where ΔV is estimated to be 29.2 cm^{-3}/mol for sulfate capacity and 6.2 cm^{-3}/mol for sulfide capacity as discussed above. We determined whether S^{2-} or S^{6+} dominates under these conditions and used either Eq. (2) or Eq. (4) to calculate sulfur fugacity. We then calculated the H_2O content of the melt at saturation using a model containing empirical compositional parameters (Moore et al. 1998). For simplicity, we assumed that the H_2O content of the melt remained at the value appropriate for saturation in pure H_2O throughout the simulation. We obtained the fugacities of H_2S, SO_2 and H_2 of the equilibrium fluids using log K values for the following reactions from the NIST–JANAF database (https://janaf.nist.gov):

$$H_2 + 0.5O_2 = H_2O(logKa = 13055/T - 2.9845)$$

$$0.5S_2 + O_2 = SO_2(logKb = 18880/T - 3.8018)$$

$$H_2S + 1.5 O_2 = H_2O + SO_2(logKc = 27103/T - 4.1973)$$

Standard states of all fluid species were taken to be the pure species at 1 bar and the temperature of interest and their mole fractions in the fluid calculated from (for SO_2 for example):
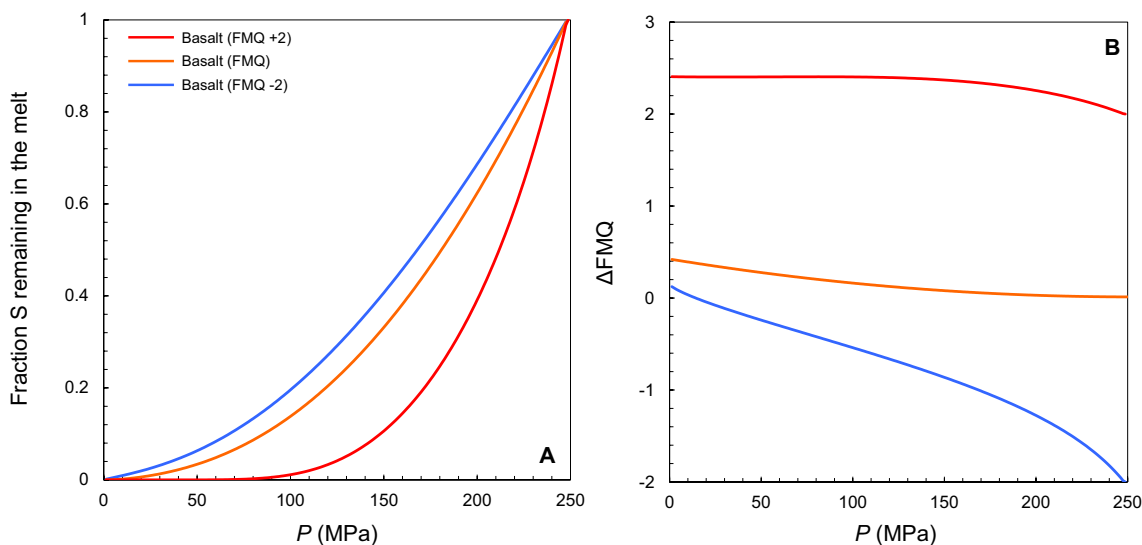

Fig. 8 **A** Degassing simulations of upwelling basaltic melts at different starting redox conditions (FMQ −2, FMQ and FMQ+2) and fixed temperature (1473 K). The simulation begins to degas H_2O-rich fluid at 250 MPa from the average basalt of Carmichael et al. (1974). The initial S content of the melt is fixed at 0.12 wt%. **B** Evolution of the redox conditions relative to the FMQ buffer during magma ascent and degassing. The FMQ buffer calculation refers to Frost (1991) model

$$X_{SO_2} = \frac{f_{SO_2}}{P \times \phi_{SO_2}} \qquad (13)$$

In Eq. (13), ϕ_{SO_2} is the fugacity coefficient of SO_2 in a mixed fluid phase of mole fraction X_{SO_2} which we assume to be dominated by H_2O. We derived values of ϕ_{SO_2} and ϕ_{H2S} for our calculations by assuming a fluid of 0.95 mol fraction H_2O and 0.05 of the relevant sulfur species. We then calculated the fugacity coefficients in the mixture from the modified Redlich–Kwong (MRK) equation of state using parameters for H_2O and H_2 from (Holloway 1977) and for SO_2 and H_2S from (Prausnitz et al. 1999). This enables us to calculate the degassing paths of melts of known initial fO_2 and known initial S content as they ascend through the crust.

We began each simulation at 250 MPa and decreased pressure in 200 steps to 1.7 MPa. At each step, the amount of H_2O released was calculated from the model of Moore et al. (1998) and the amount of S released (as H_2S and SO_2) calculated from the mole fractions of these species in the aqueous fluid. Let us consider an average basaltic magma (from Carmichael et al. 1974) at an initial fO_2 of 2 log fO_2 units above FMQ and an initial S content of 0.12% (as sulfate). This melt will start to degas SO_2 and minor H_2S and H_2 in an H_2O-dominated fluid as the melt approaches H_2O saturation. We chose to start the calculation at 250 MPa and calculated the saturated water content at 1473 K (5.1 wt% H_2O), using the empirical model of Moore et al. (1998). The initial S content of 0.12% was obtained by determining the maximum S concentration at which the melt could be undersaturated in a sulfide phase (Smythe et al. 2017). We used the H_2O saturation model to calculate the amount of H_2O exsolved from the melt into the gas phase during decompression, but made no explicit correction for the effect of H_2O on sulfate and sulfide capacity. Because degassing of sulfur is known to cause changes in fO_2 (Gaillard et al. 2011, 2015; Kelley and Cottrell 2012; Moussallame et al. 2014; Brounce et al. 2017), we calculated the fO_2 effects of degassing using the Kress and Carmichael (1991) model for Fe oxidation state. In this example, when the total amount of S dissolved as sulfate (i.e., 0.12 wt% S) is degassed principally as SO_2, the fO_2 should increase due to oxidation of FeO to Fe_2O_3. We calculate that the effect is an increase of + 0.4 units in log fO_2 from + 2 to + 2.4 log units relative to FMQ. The calculation equilibrates H_2O, H_2, H_2S and SO_2 in the gas phase and makes provision for their loss.

The volatile loss simulation (Fig. 8a) shows that the melt composition will have degassed more than 50% of its S by the time pressure reaches 200 MPa and there will be essentially none left at 80 MPa. If initial fO_2 is reduced to FMQ, the S loss rate and changes in fO_2 are reduced as H_2S becomes the dominant S species in the gas phase. In this case, the basalt will have lost 50% of its S by 175 MPa and essentially all by 30 MPa. The overall change in fO_2 during decompression is again + 0.4 log fO_2 units relative to FMQ (Fig. 8b). On reducing the initial fO_2 further to 2 log units below FMQ, there is little further change in degassing rates, although the positive change in fO_2 during degassing increases to + 2.1 log units. This is principally due to the increased mole fraction of H_2 in the gas phase, and the fact that we assume loss of H_2 from an H_2O-rich melt leaving excess O in the melt phase.

A test of the degassing simulation

Using a mixture of solubility, activity and partitioning data Ding et al. (2023) recently developed a comprehensive model (Sulfur_X) of the degassing behavior of C–O–H–S fluids from silicate melts. They applied the model to the degassing behavior of melts from Fuego, Guatemala and Mauna Kea, Hawaii. We may test the applicability of our
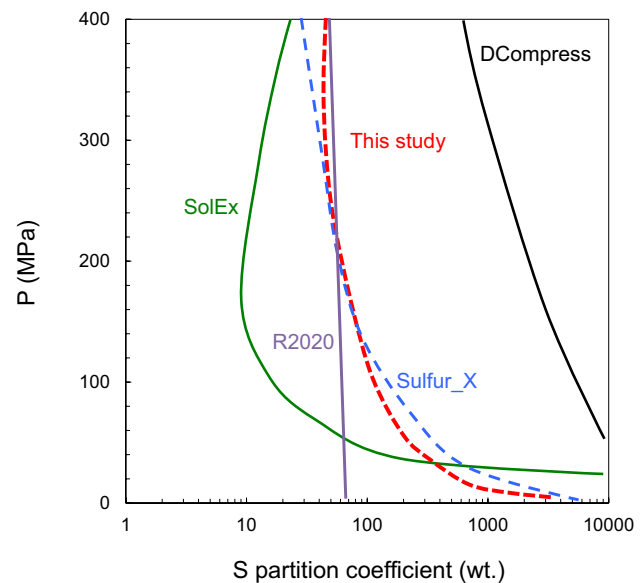

Fig. 9 Calculated partitioning of S between fluid and melt (partition coefficient = S(fluid)/S(melt) on a weight basis) for ascent of Fuego melts (from rehomogenized melt inclusions) with associated evolution of an H_2O-rich fluid. Calculated curves were taken from Fig. 8 of Ding et al. (2023) with addition of our results in red. The different models presented here are D-Compress (Burgisser et al. 2015), SolEx (Witham et al. 2012), R2020 (Rasmussen et al. 2020) and Sulfur_X (Ding et al. 2023)

simplified H–O–S model by comparing with Sulfur_X simulations of the degassing of H_2O-rich Fuego melts found as melt inclusions in olivine (Rasmussen et al. 2020).

We took a water-rich, CO_2-poor melt inclusion (FR06MI07 with 4.8% H_2O, 0.123% CO_2) and calculated the partitioning of sulfur between fluid and melt (partition coefficient D = S(fluid)/S(melt)) as this melt degasses from 400 to 0.1 MPa at a temperature of 1303 K. This simulation corresponds almost exactly to that performed by Ding et al. (2023) using the Sulfur_X model and 3 other models from the literature (Fig. 9) although in these cases CO_2 was included. As can be seen from Fig. 9, our calculated partition coefficients for S between an H_2O-rich fluid and melt correspond very closely to the Sulfur_X model and are closer to the latter than any of the models investigated by Ding et al. (2023). This agreement provides further confirmation of the strength of our data and of the validity of our degassing calculations for S-bearing, H_2O-rich fluid.

The conclusion based on our experimental measurements and simple degassing model is that SO_2 starts degassing at relatively high pressures during ascent and is virtually completely lost by 50 MPa. This is consistent with experimental results on the compositions of fluids coexisting with basalt (Lesne et al. 2011) and andesite (Fiege et al. 2014), which indicate strong degassing of S and retention of Cl at pressures below 150 MPa under oxidizing conditions. Thomas and Wood (2021) also found that Cl should be retained in basaltic melts to much lower pressures (< 2 MPa) than we find for SO_2. Degassing of S and Cl at the Soufrière Hills volcano, Montserrat (Edmonds et al. 2001), is similarly consistent with evolution of SO_2 from deep (5–7 km, 125–175 MPa) crustal magma chambers with Cl being emitted during ascent and eruption of the andesite magma.

Conclusions

We have determined sulfur solubilities and sulfide capacities of silicate melts at 50 K intervals from 1473 to 1773 K and for redox conditions below FMQ – 1.1 log fO_2 units. S contents of the quenched glasses were 200–3500 ppm and readily measureable by electron microprobe. The data obtained show increases in sulfide capacity with increasing temperature and in good agreement with previous studies (e.g., O'Neill and Mavrogenes 2002) with the FeO content of the melt (Fig. 1b).

The temperature dependence of sulfide capacity is opposite in sign to the temperature dependence of sulfate capacity

Eqs. (7, 9, 11) which means that in the temperature range 1473 K to 1773 K the fO_2 of the S^{2-} to S^{6+} transition must be temperature-dependent. We find that, relative to FMQ, the transition shifts by + 0.6 log fO_2 units as temperature decreases from 1773 to 1473 K (Fig. 4). The magnitude of the temperature effect is, however, significantly less than that proposed by Nash et al. (2019). Extrapolation to temperatures below 1473 K is complicated by the fact that sulfate capacity, as log C_{S6+}, is not, as expected, an exactly linear function of 1/T. When the nonlinearity is taken into account, calculated S^{6+}/S^{2-} for basaltic and andesitic compositions at 1323 K are, however, in good agreement with earlier measurements of Jugo et al. (2010) and Botcharnikov et al. (2011) (Fig. 5). Although the basaltic and andesitic melts generated by Jugo et al. (2010) and Botcharnikov et al. (2011) contained ~ 4–7 wt% H_2O, there is no discernable effect of H_2O on the fO_2 conditions of the S^{2-} to S^{6+} transition. Sulfide and sulfate capacities in these cases can be calculated as if the melts were anhydrous.

We find that S^{2-} is strongly stabilized relative to S^{6+} in FeO-rich melts such as those found on Mars and Vesta. This means that sulfide is stabilized in shergottitic melts to 1.5 to 2 log units above FMQ, significantly more oxidizing conditions than in terrestrial basalts.

The apparent temperatures of Fe^{3+}-Fe^{2+}-S^{6+}-S^{2-} electronic equilibrium in Mauna Kea glasses agree with the conclusions of Brounce et al. (2017) that they are quenched from near-liquidus conditions rather than re-equilibrated to lower temperatures as suggested by Nash et al. (2019).

Finally, the data from this study can be used to simulate S degassing as SO_2 and/or H_2S during magma ascent given that the effects of H_2O on sulfide and sulfate capacities are minor. If we take, for example, a basalt at temperature of 1473 K and fO_2 of FMQ, containing 0.12 wt% S and 5.1 wt% H_2O, then this basalt degasses S-rich hydrous fluid rapidly as it ascends. The basalt will have lost 50% of its S by 175 MPa and essentially all by 30 MPa. Our simplified degassing model for H–O–S fluids agrees well with the more comprehensive Sulfur_X model (Ding et al. 2023; Fig. 9) for degassing of H_2O-rich fluids from Fuego melts.

Data availability Data generated in this project are provided as an electronic supplement.

Declarations

Conflict of interest The authors declare that they have no competing financial interests.

References

Agee CB, Wilson NV, McCubbin FM, Ziegler K, Polyak VJ, Sharp ZD, Asmeron Y, Nunn MH, Shaheen R, Thiemens MH, Steele A, Fogel M, Bowden R, Glamoclija M, Zhang Z, Elardo SM (2013) Unique meteorite from early Amazonian Mars: water-rich basaltic breccia Northwest Africa 7034. Science 339(6121):780–785

Behrens H, Gaillard F (2006) Geochemical aspects of melts: volatiles and redox behavior. Elements 2(5):275–280. https://doi.org/10.2113/gselements.2.5.275

Botcharnikov RE, Linnen RL, Wilke M, Holtz F, Jugo PJ, Berndt J (2011) High gold concentrations in sulphide-bearing magma under oxidizing conditions. Nat Geosci 4(2):112–115

Boulliung J, Wood BJ (2022) SO2 solubility and degassing behavior in silicate melts. Geochim Cosmochim Acta 336:150–164. https://doi.org/10.1016/j.gca.2022.08.032

Boulliung J, Füri E, Dalou C, Tissandier L, Zimmermann L, Marrocchi Y (2020) Oxygen fugacity and melt composition controls on nitrogen solubility in silicate melts. Geochim Cosmochim Acta 284:120–133. https://doi.org/10.1016/j.gca.2020.06.020

Brounce MN, Stolper E, Eiler J (2017) Redox variations in Mauna Kea lavas, the oxygen fugacity of the Hawaiian plume, and the role of volcanic gases in Earth's oxygenation. PNAS 114(34):8997–9002. https://doi.org/10.1073/pnas.1619527114

Brounce MN, Boyce JW, McCubbin FM (2022) Sulfur in apatite from the Nakhla meteorite record a late-stage oxidation event. Earth Planet Sci Lett 595:117784. https://doi.org/10.1016/j.epsl.2022.117784

Buchanan DL, Nolan J (1979) Solubility of sulfur and sulfide immiscibility in synthetic tholeiitic melts and their relevance to Bushveld-Complex rocks. Can Min 17(2):483–494

Burgisser A, Alletti M, Scaillet B (2015) Simulating the behavior of volatiles belonging to the C–O–H–S system in silicate melts under magmatic conditions with the software D-Compress. Comput Geosci 79:1–14. https://doi.org/10.1016/j.cageo.2015.03.002

Canil D (1997) Vanadium partitioning and the oxidation state of Archaean komatiite magmas. Nature 389(6653):842–845

Carmichael ISE, Turner FJ, Verhoogen J (1974) Igneous petrology. McGraw-Hill, New York

Carroll MR, Webster JD (1994) Sulfur, noble gases, and halogens: solubility relations of the less abundant volatile species in magmas.

Reviews in mineralogy, V30. Mineralogical Society of America, pp 331–371

Chase MW Jr (1985) JANAF thermochemical tables. J Phys Chem Ref Data 14(1):1856

Ding S, Plank T, Wallace PJ, Rasmussen DJ (2023) Sulfur_X: a model of sulfur degassing during magma ascent. Geochem Geophy Geosys 24(4):e2022GC010552. https://doi.org/10.1029/2022GC010552

Edmonds M, Pyle D, Oppenheimer C (2001) A model for degassing at the Soufriere Hills Volcano, Montserrat, West Indies, based on geochemical data. Earth Planet Sci Let 186:159–173. https://doi.org/10.1016/S0012-821X(01)00242-4

Fiege A, Behrens H, Holtz F, Adams F (2014) Kinetic vs. thermodynamic control of degassing of H2O–S±Cl-bearing andesitic melts. Geochim Cosmochim Acta 125:241–264. https://doi.org/10.1016/j.gca.2013.10.012

Fincham CJB, Richardson FD (1954) The behaviour of sulphur in silicate and aluminate melts. Proc R Soc Lon Ser A Math Phy Sci 223(1152):40–62

Floran RJ, Prinz M, Hlava PF, Keil K, Nehru CE, Hinthorne JR (1978) The Chassigny meteorite: a cumulate dunite with hydrous amphibole-bearing melt inclusions. Geochim Cosmochim Acta 42(8):1213–1229. https://doi.org/10.1016/0016-7037(78)90115-1

Frost RB (1991) Introduction to oxygen fugacity and its petrologic importance. Rev Mineral Geochem 5:1–16. https://doi.org/10.1515/9781501508684-004

Gaillard F, Scaillet B (2009) The sulfur content of volcanic gases on Mars. Earth Planet Sci Lett 279(1–2):34–43. https://doi.org/10.1016/j.epsl.2008.12.028

Gaillard F, Scaillet B, Arndt NT (2011) Atmospheric oxygenation caused by a change in volcanic degassing pressure. Nature 478(7368):229–232

Gaillard F, Scaillet B, Pichavant M, Iacono-Marziano G (2015) The redox geodynamics linking basalts and their mantle sources through space and time. Chem Geol 418:217–233. https://doi.org/10.1016/j.chemgeo.2015.07.030

Haughton DR, Roeder PL, Skinner BJ (1974) Solubility of sulfur in mafic magmas. Eco Geol 69(4):451–467. https://doi.org/10.2113/gsecongeo.69.4.451

Herd CD, Papike JJ, Brearley AJ (2001) Oxygen fugacity of martian basalts from electron microprobe oxygen and TEM-EELS analyses of Fe-Ti oxides. Am Min 86(9):1015–1024. https://doi.org/10.2138/am-2001-8-908

Herd CD, Borg LE, Jones JH, Papike JJ (2002) Oxygen fugacity and geochemical variations in the Martian basalts: implications for Martian basalt petrogenesis and the oxidation state of the upper mantle of Mars. Geochim Cosmochim Acta 66(11):2025–2036. https://doi.org/10.1016/S0016-7037(02)00828-1

Hewins RH, Humayun M, Barrat JA, Zanda B, Lorand JP, Pont S, Assayag N, Cartigny P, Yang S, Sautter V (2020) Northwest Africa 8694, a ferroan chassignite: bridging the gap between nakhlites and chassignites. Geochim Cosmochim Acta 282:201–226. https://doi.org/10.1016/j.gca.2020.05.021

Holloway JR (1977) Fugacity and activity of molecular species in supercritical fluids. In: Fraser DG (ed) Thermodynamics in geology. Springer, Dordrecht, pp 161–181. https://doi.org/10.1007/978-94-010-1252-2_9

Jugo PJ, Luth RW, Richards JP (2005) Experimental data on the speciation of sulfur as a function of oxygen fugacity in basaltic melts. Geochim Cosmochim Acta 69(2):497–503. https://doi.org/10.1016/j.gca.2004.07.011

Jugo PJ, Wilke M, Botcharnikov RE (2010) Sulfur K-edge XANES analysis of natural and synthetic basaltic glasses: implications for S speciation and S content as function of oxygen fugacity. Geochim Cosmochim Acta 74(20):5926–5938. https://doi.org/10.1016/j.gca.2010.07.022

Kelley KA, Cottrell E (2012) The influence of magmatic differentiation on the oxidation state of Fe in a basaltic arc magma. Earth Planet Sci Lett 329:109–121. https://doi.org/10.1016/j.epsl.2012.02.010

Kress VC, Carmichael ISE (1991) The compressibilty of silicate liquids containing Fe2O3 and the effect of composition, temeprature, oxygen fugacity and pressure on their redox states. Cont Min Petrol 108:82–92

Lesne P, Kohn SC, Blundy J, Witham F, Botcharnikov RE, Behrens H (2011) Experimental simulation of closed-system degassing in the system basalt-H2O-CO2-S-Cl. J Petrol 52:1737–1762. https://doi.org/10.1093/petrology/egr027

Matjuschkin V, Blundy JD, Brooker RA (2016) The effect of pressure on sulphur speciation in mid-to deep-crustal arc magmas and implications for the formation of porphyry copper deposits. Cont Min Petrol 171:1–25

McSween HY Jr (2015) Petrology on mars. Am Min 100(11–12):2380–2395. https://doi.org/10.2138/am-2015-5257

Métrich N, Berry AJ, O'Neill HSC, Susini J (2009) The oxidation state of sulfur in synthetic and natural glasses determined by X-ray absorption spectroscopy. Geochim Cosmochim Acta 73(8):2382–2399. https://doi.org/10.1016/j.gca.2009.01.025

Moore G, Vennemann T, Carmichael ISE (1998) An empirical model for the solubility of H2O in magmas to 3 kilobars. Am Min 83:36–42. https://doi.org/10.2138/am-1998-1-203

Moretti R, Ottonello G (2005) Solubility and speciation of sulfur in silicate melts: the Conjugated Toop-Samis-Flood-Grjotheim (CTSFG) model. Geochim Cosmochim Acta 69(4):801–823. https://doi.org/10.1016/j.gca.2004.09.006

Moussallam Y, Oppenheimer C, Scaillet B, Gaillard F, Kyle P, Peters N, Hartley M, Berlo K, Donovan A (2014) Tracking the changing oxidation state of Erebus magmas, from mantle to surface, driven by magma ascent and degassing. Earth Planet Sci Lett 393:200–209. https://doi.org/10.1016/j.epsl.2014.02.055

Namur O, Charlier B, Holtz F, Cartier C, McCammon C (2016) Sulfur solubility in reduced mafic silicate melts: implications for the speciation and distribution of sulfur on Mercury. Earth Planet Sci Lett 448:102–114. https://doi.org/10.1016/j.epsl.2016.05.024

Nash WM, Smythe DJ, Wood BJ (2019) Compositional and temperature effects on sulfur speciation and solubility in silicate melts. Earth Planet Sci Lett 507:187–198. https://doi.org/10.1016/j.epsl.2018.12.006

Nicklas RW, Day JM, Vaci Z, Udry A, Liu Y, Tait KT (2021) Uniform oxygen fugacity of shergottite mantle sources and an oxidized martian lithosphere. Earth Planet Sci Lett 564:116876. https://doi.org/10.1016/j.epsl.2021.116876

O'Neill HSC (2005) A method for controlling alkali-metal oxide activities in one-atmosphere experiments and its application to measuring the relative activity coefficients of NaO0.5 in silicate melts. Am Min 90(2–3):497–501. https://doi.org/10.2138/am.2005.1792

O'Neill HSC (2021) The thermodynamic controls on sulfide saturation in silicate melts with application to ocean floor basalts. Magma Redox Geochem. https://doi.org/10.1002/9781119473206.ch10

O'Neill HSC, Mavrogenes JA (2002) The sulfide capacity and the sulfur content at sulfide saturation of silicate melts at 1400 C and 1 bar. J Petrol 43(6):1049–1087. https://doi.org/10.1093/petrology/43.6.1049

O'Neill HSC, Mavrogenes JA (2022) The sulfate capacities of silicate melts. Geochim Cosmochim Acta 334:368–382. https://doi.org/10.1016/j.gca.2022.06.020

Prausnitz JM, Lichtenthaler RN, Gomes de Azevedo E (1999) Molecular thermodynamics of fluid-phase equilibria, 3rd edn. Prentice Hall, New Jersey

Rasmussen DJ, Plank TA, Wallace PJ, Newcombe ME, Lowenstern JB (2020) Vapor-bubble growth in olivine-hosted melt inclusions. Am Min 105(12):1898–1919. https://doi.org/10.2138/am-2020-7377

Rezeau H, Jagoutz O (2020) The importance of H2O in arc magmas for the formation of porphyry Cu deposits. Ore Geol Rev 126:103744. https://doi.org/10.1016/j.oregeorev.2020.103744

Rubin AE, Warren PH, Greenwood JP, Verish RS, Leshin LA, Hervig RL, Clayton RN, Mayeda TK (2000) Los Angeles: the most differentiated basaltic martian meteorite. Geology 28(11):1011–1014. https://doi.org/10.1130/0091-7613(2000)28%3c1011:LATMDB%3e2.0.CO;2

Sautter V, Toplis MJ, Lorand JP, Macri M (2012) Melt inclusions in augite from the nakhlite meteorites: a reassessment of nakhlite parental melt and implications for petrogenesis. Meteor Planet Sci 47(3):330–344. https://doi.org/10.1111/j.1945-5100.2012.01332.x

Scaillet B, Luhr J, Carroll MR (2003) Petrological and volcanological constraints on volcanic sulfur emissions to the atmosphere. Geophy Mono-Am Geophy Union 139:11–40

Smythe DJ, Wood BJ, Kiseeva ES (2017) The S content of silicate melts at sulfide saturation: new experiments and a model incorporating the effects of sulfide composition. Am Min 102(4):795–803. https://doi.org/10.2138/am-2017-5800CCBY

Thomas RW, Wood BJ (2021) The chemical behaviour of chlorine in silicate melts. Geochim Cosmochim Acta 294:28–42. https://doi.org/10.1016/j.gca.2020.11.018

Tuff J, Wade J, Wood BJ (2013) Volcanism on Mars controlled by early oxidation of the upper mantle. Nature 498(7454):342–345

Wallace PJ, Carmichael IS (1994) S speciation in submarine basaltic glasses as determined by measurements of S Kα X-ray wavelength shifts. Am Min 79(1–2):161–167

Wang Z, Tian W, Di Y (2021) New temperature and oxygen fugacity data of Martian nakhlite from Northwest Africa (NWA) 5790 and implications for shallow sulphur degassing. Earth Planets Space 73(1):1–8

White WB, Johnson SM, Dantzig GB (1958) Chemical equilibrium in complex mixtures. J Chem Phy 28(5):751–755. https://doi.org/10.1063/1.1744264

Wilke M, Jugo PJ, Klimm K, Susini J, Botcharnikov R, Kohn SC, Janousch M (2008) The origin of S4+ detected in silicate glasses by XANES. Am Min 93(1):235–240. https://doi.org/10.2138/am.2008.2765

Witham F, Blundy J, Kohn SC, Lesne P, Dixon J, Churakov SV, Botcharnikov R (2012) SolEx: a model for mixed COHSCl-volatile solubilities and exsolved gas compositions in basalt. Comp Geosci 45:87–97. https://doi.org/10.1016/j.cageo.2011.09.021

Xu Z, Li Y (2021) The sulfur concentration at anhydrite saturation in silicate melts: implications for sulfur cycle and oxidation state in subduction zones. Geochim Cosmochim Acta 306:98–123. https://doi.org/10.1016/j.gca.2021.05.027